PHYSICAL REVIEW FLUIDS **4**, 034802 (2019)

Editors' Suggestion

Excitation and resonant enhancement of axisymmetric internal wave modes

S. Boury,[1] T. Peacock,[2] and P. Odier[1]

[1]*Univ Lyon, ENS de Lyon, Univ Claude Bernard, CNRS, Laboratoire de Physique, F-69342 Lyon, France*

[2]*Department of Mechanical Engineering, Massachusetts Institute of Technology, Cambridge, Massachusetts 02139, USA*

(Received 23 October 2018; published 5 March 2019)

To date, axisymmetric internal wave fields, which have relevance to atmospheric internal wave fields generated by storm cells and oceanic near-inertial wave fields produced by surface perturbations, have been experimentally realized using an oscillating sphere or torus as the source. Here we use a wave generator configuration capable of exciting axisymmetric internal wave fields of arbitrary radial form to generate axisymmetric internal wave modes. After establishing the theoretical background for axisymmetric mode propagation, taking into account lateral and vertical confinement, and also accounting for the effects of weak viscosity, we study modes of different order. We characterize the efficiency of the wave generator through careful measurement of the wave amplitude based upon group velocity arguments, and then consider the effect of vertical confinement to induce resonance, identifying a series of experimental resonant peaks that agree well with theoretical predictions. In the vicinity of resonance, the wave fields undergo a transition to nonlinear behavior that is initiated on the central axis of the domain and proceeds to erode the wave field throughout the domain.

DOI: 10.1103/PhysRevFluids.4.034802

I. INTRODUCTION

Since the early studies of Görtler [1] and Mowbray and Rarity [2], laboratory experiments have played a central role in the development of understanding of internal wave fields. Initially, much of the focus was on two-dimensional internal wave beams generated by excitation methods such as an oscillating cylinder [2,3] or moving topography [4,5]. For modeling purposes, such a wave field can be treated as nominally invariant in the transverse direction and thus described in terms of plane waves *via* Fourier transforms [6,7].

Inspired by oceanographic studies, and building on earlier experiments that used paddle generators to excite vertical [8] or horizontal [9,10] modes, novel internal wave generator technology [11] has been used for a variety of studies of two-dimensional internal wave modes. We define modes as standing waves produced *via* the interference between two waves of the same magnitude but different directions. In doubly confined geometries (i.e., sidewalls, top and bottom), two-dimensional modes of different orders, determined by the combination of stratification, imposed frequency, and dimensions of confinement, have been studied [7,12]. The capability of the novel generator technology to investigate wave beams and two-dimensional modes was thoroughly explored by Mercier *et al.* [13]. Such capabilities have been employed to investigate, for example, the triadic resonant instability (TRI) in a vertical mode propagating horizontally [14] or the formation of multilayered stratifications [15]. While theoretical studies for linear stratifications describe such wave fields in terms of the natural modal basis of sines and cosines, it should be recalled that the modal pattern can be considered as a combination of plane waves propagating and reflecting from the system boundaries [13].

Axisymmetric wave fields have traditionally been experimentally excited using a vertically oscillating sphere and exploring the shape of the wave beams [16–21]. While the form of the wave field close to the oscillating body is nontrivial, modeling studies have explored the limit states of the wave beams in terms of plane waves with a spherical amplitude decreasing as $r^{-1/2}$, r being the radial distance from the sphere, computed from the Green function of the moving source [22], or as infinite sums of Bessel functions with complex coefficients [7,23]. The amplitude decrease and the viscous decay of the conical wave beam emitted by an oscillating sphere has been explored in laboratory experiments by Flynn *et al.* [17] showing good agreement with theoretical predictions. More sophisticated axisymmetric experimental geometries have been investigated using a vertically and a horizontally oscillating torus, respectively [24,25], in which case a highly nonlinear process occurs due to the three-dimensional geometric focusing, able to transport momentum and break into turbulence. None of these experimental configurations, however, readily permitted a change in the form or the wave number of the wave field being excited.

In Ref. [26], Maurer *et al.* developped an axisymmetric wave generator, adapted from its planar counterpart [11] by using oscillating concentric cylinders instead of parallel plates. It has been used to generate high-fidelity axisymmetric internal wave fields, with substantial flexibility in the setting of the radial wavelength. Studies using this technology reveal axisymmetric wave cones propagating in the stratified medium according to the internal wave dispersion relation and with radial profiles imposed by the configuration of the generator, such as ring-shaped excitation or truncated Bessel functions [26]. Wave amplitudes and frequencies were measured, showing a good agreement with the linear theory for axisymmetric waves in a stratified fluid of constant buoyancy, in both the nonrotating and rotating cases.

To date, there have been no experimental studies of internal wave modes in an axisymmetric geometry. Furthermore, to our knowledge, there is no quantitative study of resonant confined modes, even in two-dimensional geometries. In this paper we perform laboratory experimental realizations of axisymmetric modes. In Sec. II we establish the general theory for axisymmetric modes of internal waves by considering both radial and vertical confinement as well as weakly viscous effects. Then in Sec. III we describe our experimental apparatus, adapted from Maurer *et al.* [26]. Experimental results are presented in Sec. IV, followed by conclusions and discussion in Sec. V.

II. THEORY

A. Governing equations

In a cylindrical framework $(\mathbf{e_r}, \mathbf{e}_\theta, \mathbf{e_z})$, with $\mathbf{e_z}$ vertically upwards, small-amplitude inertia gravity waves in an inviscid fluid with a constant background stratification satisfy the following equations in the Boussinesq approximation:

$$\rho_0\left[\frac{\partial \mathbf{v}}{\partial t} + (\mathbf{v}\cdot\boldsymbol{\nabla})\mathbf{v}\right] = -\boldsymbol{\nabla} p - (\rho - \bar{\rho})g\mathbf{e_z}, \tag{1}$$

$$\frac{\partial \rho}{\partial t} + (\mathbf{v}\cdot\boldsymbol{\nabla})\rho = 0, \tag{2}$$

$$\boldsymbol{\nabla}\cdot\mathbf{v} = 0, \tag{3}$$

where $\mathbf{v} = (v_r,\ v_\theta,\ v_z)$ is the velocity field, p the pressure field, ρ the density field, and $\bar{\rho}$ the background density field. We define the buoyancy frequency N *via* the relation $N^2 = (-g/\rho_0)\partial\bar{\rho}/\partial z$ with ρ_0 being a reference density.

Considering axisymmetric wave fields, we assume that there is no variation in the azimuthal direction and hence all functions depend only on (r, z, t). By introducing the axisymmetric stream function ψ such that

$$v_r = -\frac{1}{r}\frac{\partial(r\psi)}{\partial z} \quad \text{and} \quad v_z = \frac{1}{r}\frac{\partial(r\psi)}{\partial r}, \tag{4}$$

Eqs. (1), (2), and (3) become

$$\partial_t^2\left\{\partial_z^2\psi+\partial_r\left[\frac{1}{r}\partial_r(r\psi)\right]\right\}+N^2\partial_r\left[\frac{1}{r}\partial_r(r\psi)\right]=0. \tag{5}$$

Natural axisymmetric solutions of this equation can be found through a Fourier-Hankel decomposition. Using a modal basis, the solutions write as linear combinations of Bessel functions of the first kind J_1 and of the second kind Y_1. The latter has a singularity at $r=0$ so only the J_1 function will be considered. As different radial wave numbers may enter in the decomposition, the stream function ψ can then be written as a modal sum

$$\psi(r,z,t)=\iint\phi(z)J_1(lr)\exp(-i\omega t)\,dl\,d\omega. \tag{6}$$

Radial and vertical velocities can be derived from Eq. (6) using classic relations for the Bessel derivatives, as follows:

$$v_r(r,z,t)=\iint\phi'(z)J_1(lr)\exp(-i\omega t)\,dl\,d\omega, \tag{7}$$

$$v_z(r,z,t)=\iint l\phi(z)J_0(lr)\exp(-i\omega t)\,dl\,d\omega. \tag{8}$$

For a given frequency ω and radial mode l, $\phi(z)$ satisfies

$$\omega^2\phi''(z)-l^2(N^2-\omega^2)\phi(z)=0. \tag{9}$$

Solutions of Eq. (9) are exponential functions, either complex or real. They can be either propagative or evanescent waves, depending on the frequency, as long as the vertical wave number m satisfies the dispersion relation

$$m^2=l^2\frac{N^2-\omega^2}{\omega^2}. \tag{10}$$

If we define $\beta=\sin^{-1}(l/k)$ to be the angle between the vertical axis and the wave vector $\mathbf{k}=(l,0,m)$ of magnitude $k=\sqrt{l^2+m^2}$, the dispersion relation (10) simplifies in

$$\sin\beta=\pm\frac{\omega}{N}. \tag{11}$$

According to Eq. (11), internal gravity waves propagate along a direction fixed by the angle β. In a two-dimensional geometry, four wave beams on a St Andrew's cross are formed [2,3]. In a three-dimensional axisymmetric geometry, the dispersion relation sets two cones aligned along the vertical direction and connected by the apex [7,20].

B. Radial confinement

In a previous study, Maurer *et al.* [26] analyzed the production of a conical wave field generated by an axisymmetric moving form at the surface, for which the radial profile was a truncated Bessel function. Although Bessel functions form a natural basis of study for axisymmetric wave fields, the analytical form of the wave field for a truncated Bessel function is not so simple. An illustration is presented in Fig. 1(a), which displays a vertical cut of the spatial structure of the wave field studied in Ref. [26]. Immediately below the generator [region 1 in Fig. 1(a)], the wave field preserves its radial form, but further below, the wave field develops a conical beam-shaped profile (region 2), which can locally be modeled by a plane wave. Finally, due to the propagation angle set by (11), sufficiently far below the oscillating body around the vertical axis the wave field is absent (region 3). Analytically, this evolution of the wave field is a natural consequence of the truncated Bessel function forcing being expressed as an integral over Bessel functions of different wavelengths, with coefficients

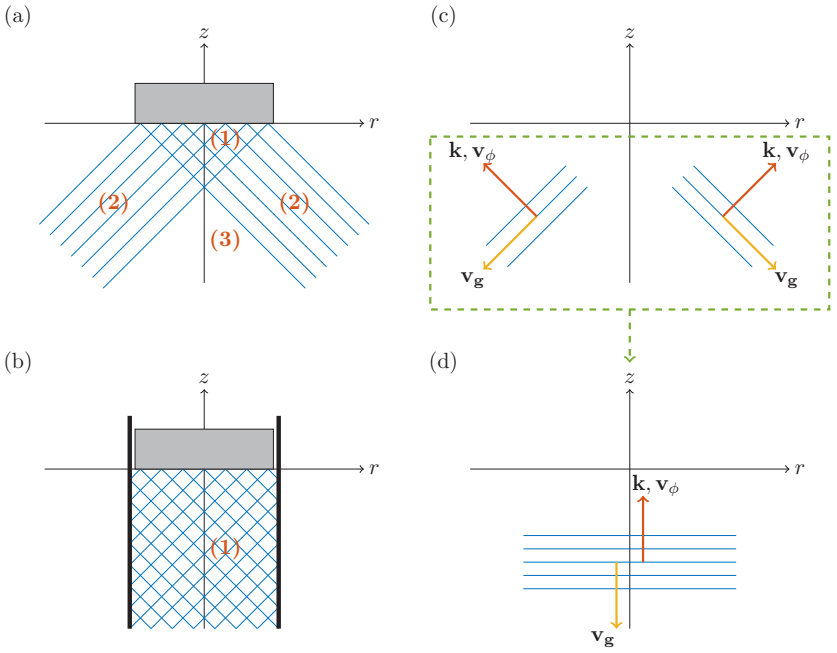

FIG. 1. Left: Beams for downwards propagating wave generation in (a) unconfined and (b) confined geometries produced by a wave generator or an oscillating body (light gray rectangle). Right: (c) Phase lines of two different wave beams allowed by the dispersion relation and (d) phase lines of the wave rerecombination for vertically propagating horizontal (radial) modes. The reader is directed to Fig. 2 or Ref. [26] for practical details on the wave generation process.

depending on the spatial forcing. Complex models have been set up to understand the nature of such radiated wave fields [17,23,27].

Given the finite spatial extent of the forcing, to generate a modal wave field described by a single radial Bessel function, confinement can be imposed experimentally to the fluid, as illustrated in Fig. 1(b). As for planar geometries, confinement prevents the wave from propagating in the bounded direction. Given the assumption of axisymmetry, we seek a wave field that is radially confined by a cylinder of radius R equal to the radius of the generator, and vertically propagating, which is in contrast to the planar scenario that has vertical confinement and permits lateral propagation [13–15]. We impose the radial boundary condition

$$v_r(r = R, z) = \left(\frac{\partial \psi}{\partial z}\right)_{(r=R,z)} = 0, \tag{12}$$

which means that $\psi(r = R, z)$ is a constant, corresponding to a maximum of vertical velocity and a vanishing radial velocity at the outer boundary, and conserving volume in the domain. Condition (12) limits possible values of the radial wave number l, as the product lR has to be a zero of the J_1 Bessel function, and if the fluid is excited with one of these wave numbers at frequency ω, a single propagating mode is expected to result.

Figure 1(c) shows the two directions of propagation allowed for the wave beams by the dispersion relation (11), in a vertical planar cross section, for a wave generation at the surface. In our experiment, the radial confinement leads to downward propagating modes which are, as depicted in Figs. 1(c) and 1(d) (still in a vertical planar cross section) a recombination of conically propagating beams. Due to the symmetry with respect to the vertical axis, the radial direction of propagation

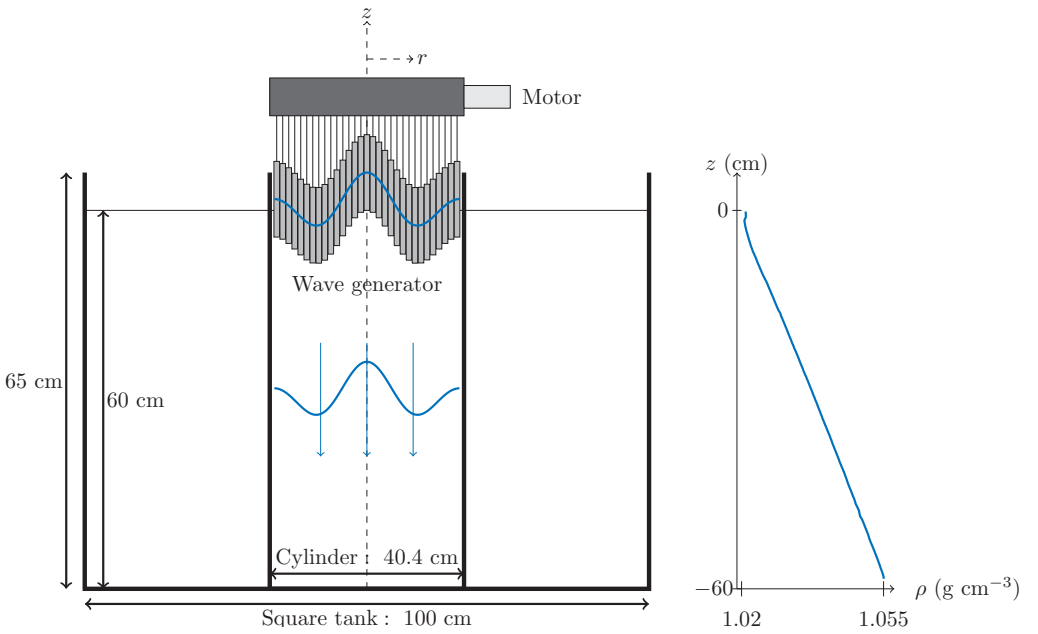

FIG. 2. Schematic of the experimental apparatus. Left: A cylindrical tank, inside a square tank, confines the waves produced by the generator located at the surface, leading to a radial Bessel mode propagating downwards. Right: Example of linear stratification measured in the experiments. Vertical dimension of the generator is not to scale.

cancels out, and, for a downwards propagating wave at a selected frequency ω and wave number $\mathbf{k}$, the phase and group velocities can be computed from the dispersion relation (11):

$$\mathbf{v}_\phi = \frac{1}{2\pi}\int_0^{2\pi} \frac{Nl}{k}(l\mathbf{e_r} + m\mathbf{e_z})\,d\theta = \frac{Nlm}{k}\mathbf{e_z}, \tag{13}$$

$$\mathbf{v_g} = \frac{1}{2\pi}\int_0^{2\pi} \frac{mlN^2}{\omega k^4}(m\mathbf{e_r} - l\mathbf{e_z})\,d\theta = -\frac{ml^2N^2}{\omega k^4}\mathbf{e_z}. \tag{14}$$

Equations (13) and (14) show phase and group velocity oriented in opposite directions, illustrated in Fig. 1(d), consistent with oceanic signatures identified by oceanographers looking for internal waves [28,29]. This feature contrasts with horizontally propagating modes, relevant only in Cartesian geometry, which show phase and group velocities pointing towards the same direction [13].

To investigate the shape of the wave field in the experimental domain, and more specifically its amplitude, we extend the axisymmetric analysis of Sutherland [7, ch. 5], first derived for an oscillating cylinder in a two-dimensional geometry, by applying it to our axisymmetric flat generator in a confined domain. Through a Fourier transform, the time dependency of the stream function can be expressed in complex coordinates as $\psi \propto e^{-i\omega t}$, the velocity field being the real part of the stream function derivatives. Neglecting rotation and introducing $\Gamma^2 = 1 - N^2/\omega^2$, Eq. (5) can be rewritten

$$\Gamma^2 \frac{\partial}{\partial r}\left[\frac{1}{r}\frac{\partial(r\psi)}{\partial r}\right] + \frac{\partial^2\psi}{\partial z^2} = 0. \tag{15}$$

Considering that the cylindrical plates of the generator are moving vertically (as shown in Fig. 2, and detailed in Ref. [26]) and are injecting a vertical velocity $a\omega$, with a being a sufficiently small

displacement so that the fluid surface can be considered to reside at $z = 0$, the boundary conditions that apply to the stream function field are

$$v_z(r, z = 0) = \left[\frac{1}{r}\frac{\partial(r\psi)}{\partial r}\right]_{(r,z=0)} = a\omega J_0(lr), \tag{16}$$

$$v_r(r = R, z) = \left(\frac{\partial\psi}{\partial z}\right)_{(r=R,z)} = 0. \tag{17}$$

Equation (16) means that the generator imposes its own movement to the fluid at the top of the domain. The modal boundary condition is expressed by Eq. (17) as detailed before.

For $\omega > N$, the problem can be readily solved *via* a coordinate transformation: ($r' = \Gamma r$, $z' = z$) so that Eq. (15) becomes

$$\Delta'_h\psi = 0, \tag{18}$$

where Δ'_h is the horizontal Laplacian. The solution can be obtained using separation of variables. The radial part of the equation satisfies a Bessel differential equation of first order, leading to $\psi \propto J_1(lr)$. The vertical component is found to be exponential [see Eq. (9)], and $\psi \propto \exp(\Gamma lz)$ as the amplitude decreases as z goes to $-\infty$. From the boundary conditions, the different coefficients can be set. Recasting the solution in the original coordinates, we obtain

$$\psi_{\omega>N}(r, z, t) = -\frac{a\omega}{l}J_1(lr)\exp(mz)\cos(\omega t), \tag{19}$$

where we define $m = \Gamma l$, which contains the influence of the stratification.

In the case $\omega < N$, the term $1 - N^2/\omega^2$ is negative. We thus define $\gamma^2 = \frac{N^2}{\omega^2} - 1$, and, by analytic continuation, the problem can be solved using the same method as before. Because of the second-order derivatives, the problem remains well defined, though we are using complex analysis and the final stream function belongs to the real space of functions

$$\psi_{\omega<N}(r, z, t) = -\frac{a\omega}{l}J_1(lr)\cos(mz - \omega t), \tag{20}$$

with m the vertical wave number defined as $m^2 = \gamma^2 l^2$. Hence, we obtain two different radial modes, one being evanescent (19) and the other one propagating in the vertical direction (20).

Henceforth, we are considering only the case of propagative waves with $\omega < N$. The vertical velocity being a radial derivative of ψ, it behaves as $v_z \propto a\omega$:

$$v_z(r, z, t) = \frac{1}{r}\frac{\partial(r\psi)}{\partial r} = a\omega J_0(lr)\cos(mz - \omega t), \tag{21}$$

$$v_r(r, z, t) = \frac{\partial\psi}{\partial z} = -\frac{a\omega m}{l}J_1(lr)\sin(mz - \omega t). \tag{22}$$

C. Vertical confinement

In our experiments, boundaries at the top ($z = 0$) and at the bottom ($z = -L$) are to be taken into account. This confinement creates a finite domain where a behavior similar to an opto-electromagnetic cavity [30] or a Melde's string for acoustic or mechanical waves [31] can take place, with different modes and resonances. The total wave field in the cavity is obtained by a superposition of all the reflected waves, from the top and the bottom of the tank, causing constructive or destructive interferences. In this configuration, the generator is continuously exciting a velocity field given by a stream function ψ_1, described in complex notation by

$$\psi_1(r, z, t) = \psi_1^0 J_1(lr)e^{i(\omega t - mz)}, \tag{23}$$

with $\psi^0 = a\omega/l$. At $z = -L$, the downwards wave field ψ_1 is reflected into an upwards wave field ψ_2, and at $z = 0$, the ψ_2 stream function is reflected into another downwards wave ψ_3. Repeated

reflections occur at $z = 0$ and $z = -L$, and as a result the total stream field is composed of an infinite sum of reflected wave fields.

We denote by odd numbers the downwards waves and by even numbers the upwards waves. At the boundaries, as well as changing direction, reflection also induces a π phase shift, and if we assume that there is no dissipation, the amplitudes of the stream functions are equal before and after reflection. Boundary conditions at the top and at the bottom of the tank then apply as

$$\psi_{2k-1}(z = -L) = \psi_{2k}(z = -L)e^{i\pi}, \tag{24}$$

$$\psi_{2k+1}(z = 0) = \psi_{2k}(z = 0)e^{i\pi}, \tag{25}$$

leading to

$$\psi^0_{2k} = \psi^0_{2k-1}e^{-2imL-i\pi}, \tag{26}$$

$$\psi^0_{2k} = \psi^0_{2k+1}e^{i\pi}. \tag{27}$$

We deduce that the general expression of these wave amplitudes are

$$\psi^0_{2k} = \psi^0_1 e^{-2ikmL+(2k-1)\pi}, \tag{28}$$

$$\psi^0_{2k+1} = \psi^0_1 e^{-2ikmL+(2k)\pi}. \tag{29}$$

As the tank undergoes an infinite number of wave reflections, we describe the total wave field by a sum over all the reflected waves

$$\psi = \sum_{k=1}^{\infty} \psi_k = \psi^0_1 J_1(lr)e^{i\pi/2}e^{i\omega t}\frac{\sin[m(z-L)]}{i\sin(mL)}, \tag{30}$$

hence the real field becomes

$$\Re(\psi) = \psi^0_1 J_1(lr)\frac{\cos(\omega t)\sin[m(z-L)]}{\sin(mL)}. \tag{31}$$

Waves that contribute to the total wave field interact either constructively or destructively. In the first case, we would be able to define a temporal and a spatial period, fixed by the wave parameters ω, l, and m, and by the size of the cavity L, as in any wave resonator. Exact cavity modes are obtained if the reflection at $z = -L$ produces a reflected wave in phase with the incoming wave, which means that this position is already a node of the wave field. This resonance condition can be expressed as

$$L = n\frac{\lambda}{2}, \quad \text{for} \quad n \in \mathbb{N}, \tag{32}$$

with $\lambda = 2\pi/m$ being the vertical wavelength. A direct consequence is that the reflection at $z = 0$ also produces a wave in phase with the incoming wave, so all reflected waves will be interacting constructively. Therefore, this relation can be written as a condition involving resonant frequencies ω_n:

$$\frac{\omega_n}{N} = \frac{(Ll)^2}{\pi^2 n^2 + (Ll)^2}. \tag{33}$$

Similar to electromagnetic waves, the cavity operates as a frequency selector, as a discrete number of frequencies ω_n fulfills the resonance condition. We present in Table I a list of the first 10 resonant frequencies that can be selected in a radial mode 1 configuration with $L = 60\,\text{cm}$ and $l = 19\,\text{m}^{-1}$.

TABLE I. First 10 resonant frequencies computed for $L = 60\,\text{cm}$ and $l = 19\,\text{m}^{-1}$.

n	0	1	2	3	4	5	6	7	8	9	10
ω_n/N	1	0.964	0.876	0.771	0.672	0.588	0.518	0.460	0.413	0.374	0.341

D. Weakly viscous correction

In the preceding derivations, an inviscid fluid was assumed. This made possible the propagation of a single mode at all frequencies without a damping effect and the existence of exact resonant cavity modes. As we will see, however, such an approximation is relevant only for a selected range of frequencies. To quantify the viscous effects on the wave propagation, we write the vertical wave number as the following expansion:

$$m = m^{(0)} + i\varepsilon m^{(1)} + O(\varepsilon^2), \tag{34}$$

with $\varepsilon = \nu l^2/\omega$, $m^{(0)}$ being the inviscid wave number [Eq. (10)] and $m^{(1)}$ being the first order correction. Including viscous terms, Eq. (9) becomes

$$\phi^{(4)}(z) - \left(2l^2 - i\frac{\omega^2}{\nu}\right)\phi''(z) + l^2\left(l^2 + i\frac{N^2-\omega^2}{\nu\omega}\right)\phi(z) = 0. \tag{35}$$

Hence, with the vertical dependence being $\exp(imz)$ [complex notation of Eq. (20)] and m defined as in Eq. (34), one can extract from Eq. (35) the following weakly viscous correction:

$$i\varepsilon m^{(1)} = \mp\frac{i\varepsilon l}{2\alpha^3\sqrt{1-\alpha^2}}, \tag{36}$$

where $\alpha = \omega/N$. Hence, at an altitude z below the wave generation source, the weakly viscous stream function ψ_ν writes

$$\psi_\nu(z) = \psi(z)\exp(-\varepsilon m^{(1)}|z|). \tag{37}$$

According to Eq. (37), the typical vertical length of viscous damping $1/\varepsilon m^{(1)}$ depends on the frequency ω and is smaller at low frequencies than at high frequencies. These results will help us to understand experimental measurements of the wave field amplitudes when comparing them to the velocity amplitudes of the generator.

III. EXPERIMENTAL APPARATUS

To conduct our experiments, the experimental setup of Maurer *et al.* [26] was adapted. A general schematic of the experimental apparatus is presented in Fig. 2. We introduce natural cylindrical coordinates with the origin taken at the surface of the water at the center of the tank.

The generator comprises 16, 12-mm-thick, concentric PVC cylinders periodically oscillating, each of them being forced by two eccentric cams. The eccentricities can be configured to introduce a phase shift between the different cylinders, and the oscillating amplitude can be set for each individual cylinder. As a result, the vertical displacement of the nth cylinder can be described by

$$a_n(t) = A_n\cos(\omega t + \alpha), \tag{38}$$

with A_n its amplitude, ω the forcing frequency, and α a phase shift. For a smooth motion of the PVC cylinders, a 1 mm gap is kept between each cylinder, and the total diameter of the wave generator is then 402 mm. The generator is mounted at the surface of the water to force downwards internal waves.

To investigate the ability of this experimental setup to produce modal wave fields, we set the generator in three different configurations to excite first-, second-, and third-order modes. Modes are defined by the number of nodes of the Bessel function present in the range $r \in [0; 20]\,\text{cm}$ (size

TABLE II. Steepness la of the profile, and amplitudes (in mm) of the different cams of the generator in the different mode profiles we used. The first cam is located at $r = 0$.

Cams	Steepness	1	2	3	4	5	6	7	8	9	10	11	12	13	14	15	16
Mode 1 (high-amplitude)	0.095	5	4.9	4.7	4.3	3.9	3.3	2.6	1.9	1.2	0.5	−0.2	−0.6	−1.2	−1.6	−1.9	−2
Mode 1 (low-amplitude)	0.048	2.5	2.4	2.3	2.1	1.9	1.6	1.3	0.9	0.6	0.2	−0.1	−0.3	−0.6	−0.8	−0.9	−1
Mode 2	0.175	5	4.7	4	2.9	1.6	0.3	−0.8	−1.6	−2	−1.9	−1.5	−0.9	−0.1	0.6	1.2	1.5
Mode 3	0.255	5	4.5	3	1.2	−0.6	−1.7	−2	−1.4	−0.4	0.7	1.4	1.5	0.9	0	−0.8	−1.2

of the generator). It sets the radial wavelength, and we computed the three associated wave numbers: $l_1 = 19\,\mathrm{m}^{-1}$, $l_2 = 35\,\mathrm{m}^{-1}$, and $l_3 = 51\,\mathrm{m}^{-1}$. We did not look for modes of higher orders because the discretization of the generator profile would not be sufficient to produce smooth enough shapes of Bessel functions. In addition, coarse discretization of high modes might severely compromise the volume-preserving nature of a Bessel function that is approximately preserved for low modes. The amplitudes of the different cams for the three modes are summarized in Table II. The profiles can be defined by the radial wave number l and the amplitude at $r = 0$ that we call a. The different amplitudes a_n, for $n \neq 0$, are taken to be the discrete approximation of the Bessel function defined by l and a. The steepness of the profile is defined as the product la.

Experiments were conducted in a cylindrical acrylic tank. To respect the boundary condition (12), the tank is of the same diameter as the generator. This transparent cylindrical tank was set into a square acrylic tank to prevent the experiment visualization suffering from optical deformations that would occur due to the curved interface created by the cylinder. Both tanks were filled with salt-stratified water with the same density profile. We used the double-bucket method to fill the tanks with a linear stratification [32,33]. Density and buoyancy were measured as a function of depth using a calibrated PME conductivity and temperature probe mounted on a motorized vertical axis. Buoyancy frequency is estimated from the mean value of the N profile obtained from the density function $\rho(z)$ measured from the free surface to within a couple of centimeters of the bottom of the tank, due to the construction of the probe. The wave generator was immersed at a depth of 2 cm into the stratification. Errors on the buoyancy frequency are estimated using the standard deviation of this N profile and are in most cases about 4% of the estimated N value. We used buoyancy frequencies in the range $N \approx 0.6\,\mathrm{rad\,s}^{-1}$ to $N \approx 1\,\mathrm{rad\,s}^{-1}$.

Velocity fields were obtained via particle image velocimetry (PIV). A laser sheet was created by a laser beam (Ti:Sapphire, 2 W, wavelength 532 nm) going through a cylindrical lens. It could be oriented either horizontally (to measure the radial and orthoradial velocity) or vertically (to measure the vertical and radial velocity). For the purpose of visualization, 10 μm diameter hollow glass spheres of volumetric mass $1.1\,\mathrm{kg\,L}^{-1}$ were added to the fluid while filling the tank. To obtain good quality velocity fields near the bottom of the tank and while imaging in a horizontal plane, 10 μm silver-covered spheres of volumetric mass $1.4\,\mathrm{kg\,L}^{-1}$ were added when needed in some experiments. Images were recorded at 1 Hz, and data processing of the PIV raw images was done using the CIVx algorithm [34].

IV. RESULTS

A. Radial modes

Figure 3 presents a summary of the experimental PIV results for the generation of modes 1 through 3 in a linear stratification with $\omega/N = 0.6$ for modes 1 and 2 and $\omega/N = 0.65$ for mode 3, and a generator amplitude $a = 5$ mm. The generator plate configuration for each mode is illustrated in the left-hand column, with n nodes for mode n. The vertical cross-sectional plots of the vertical

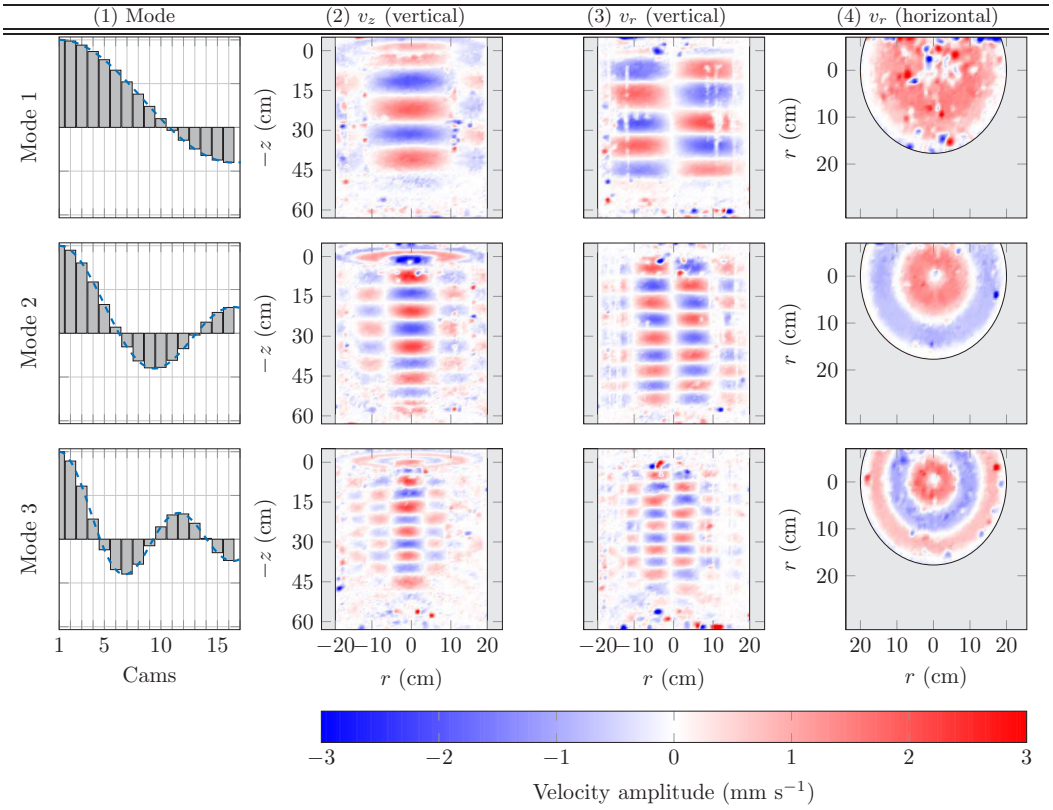

FIG. 3. Radial modes 1, 2, and 3, as observed in PIV in the experiment. First column: generator configuration that sets the mode. Second column: vertical velocity in a vertical plane. Third and fourth columns: radial velocity in a vertical and in a horizontal plane around middepth. Shaded areas are outside of the confining cylinder. For the purpose of visualization, negative values of r are used in the vertical PIV plane, leading to antisymmetric radial velocities as predicted by Eq. (22).

velocity, presented in column 2, possess the horizontal structure of the generator, increasingly intricate for the higher modes, with associated vertical sequences of maxima and minima. Columns 3 and 4 in Fig. 3 present vertical and horizontal cross sectional plots of the radial velocity component. For every mode, the radial velocity structure possesses a left-right antisymmetry in the vertical plane. The different nodes of radial velocity, which correspond to antinodes of vertical velocity, are also clearly visible in plots of the velocity in the horizontal plane, presented in column 4; these images also show the form of the generator being reproduced by the underlying wave field. No orthoradial velocity v_θ was observed in the horizontal plane.

In a previous study, Maurer *et al.* [26] experimentally measured the internal wave dispersion relation for freely propagating waves generated by an axisymmetric wave generator with no lateral confinement, which was consistent with theoretical predictions. In the modal configuration, however, the dispersion relation does not explicitly contain an angle of propagation, only a statement of the vertical wavelength as a function of the forcing frequency and horizontal wave number. The vertical wave number m was measured for different frequencies ω/N for the three modes in our experiments. Figure 4 compares the experimental values of m with the theoretical one extracted from Eq. (10) given the control parameters. Measurements were performed by looking at the spatial vertical period of the vertical velocity on PIV images. It shows a good agreement for the three modes considered in the study, though there is a slight deviation at low frequencies, probably because of

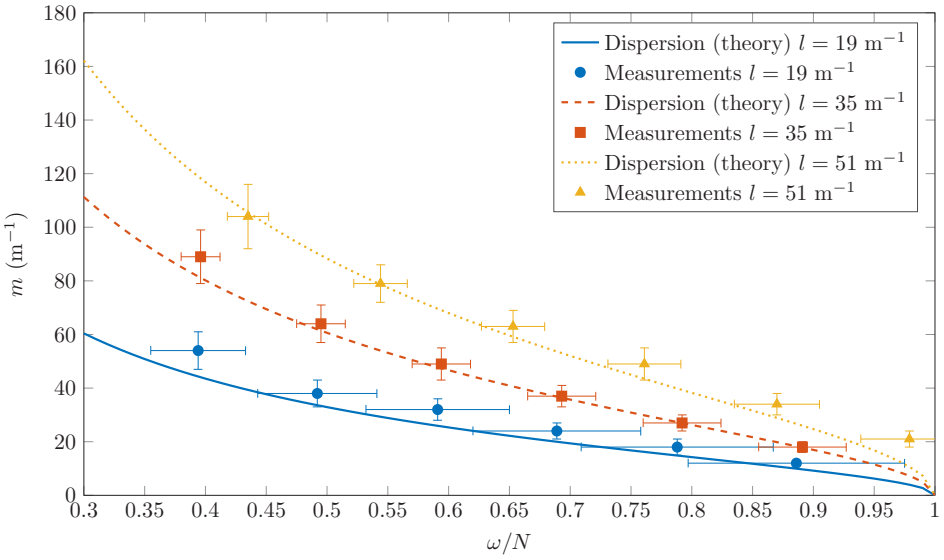

FIG. 4. Measured values of the vertical wave number (data points) for modes 1, 2, and 3, compared to the theoretical expectations from Eq. (10) (lines). Vertical errors were determined using measurements of m at different times, and horizontal errors using the standard deviation on the buoyancy frequencies from the probe profiles.

the error in N, which was about 10% for mode 1 experiment and 4% for mode 2 and mode 3 experiments.

To quantitatively investigate how close the experiments reproduce the theoretical modal Bessel profile, Fig. 5 presents radial profiles of v_z and v_r, fitted to the expected radial dependency of the Bessel mode, for mode 1, mode 2, and mode 3 configurations. We see that $v_z(r) \propto J_0(lr)$ and $v_r(r) \propto J_1(lr)$, with $l = 19\,\mathrm{m}^{-1}$, $35\,\mathrm{m}^{-1}$, or $51\,\mathrm{m}^{-1}$, as expected; these horizontal structures are preserved through the vertical propagation of the wave field. Small deformations sometimes appear close to the boundaries at $r = 20\,\mathrm{cm}$, due to boundary layer effects. The perturbation observed symmetrically around $12\,\mathrm{cm} < |r| < 16\,\mathrm{cm}$ is actually caused by laser reflections in the cylinder, producing locally poor PIV visualization.

B. Generator efficiency

The efficiency of the wave generator, being the ratio of the amplitude of the waves produced to the amplitude of the generator motion, is investigated in order to characterize the quality of the produced wave field. Hence, it is essential to reliably measure the amplitude of the internal wave field, which is, due to unavoidable reflections in closed domains, a delicate task and more challenging than measuring their frequency or wavelength.

A few previous studies have made direct measurements of velocity amplitude, although these are typically done either at high frequencies or relatively high amplitudes. Mathur and Peacock [35] studied transmission and reflection of internal wave beams across a transmission region and took a Fourier transform of the reflected and transmitted wave fields along appropriately chosen transects, Maurer [36] measured wave amplitudes by looking at the maximum of the velocity over a given spatial area, and Supekar [37] utilized the distribution of maxima of amplitudes for a velocity field in a widespread two-dimensional beam. In performing our experiments, it was necessary to more rigorously define our amplitude measurement methodology based on understanding of the group velocity of the wave fields we were studying.

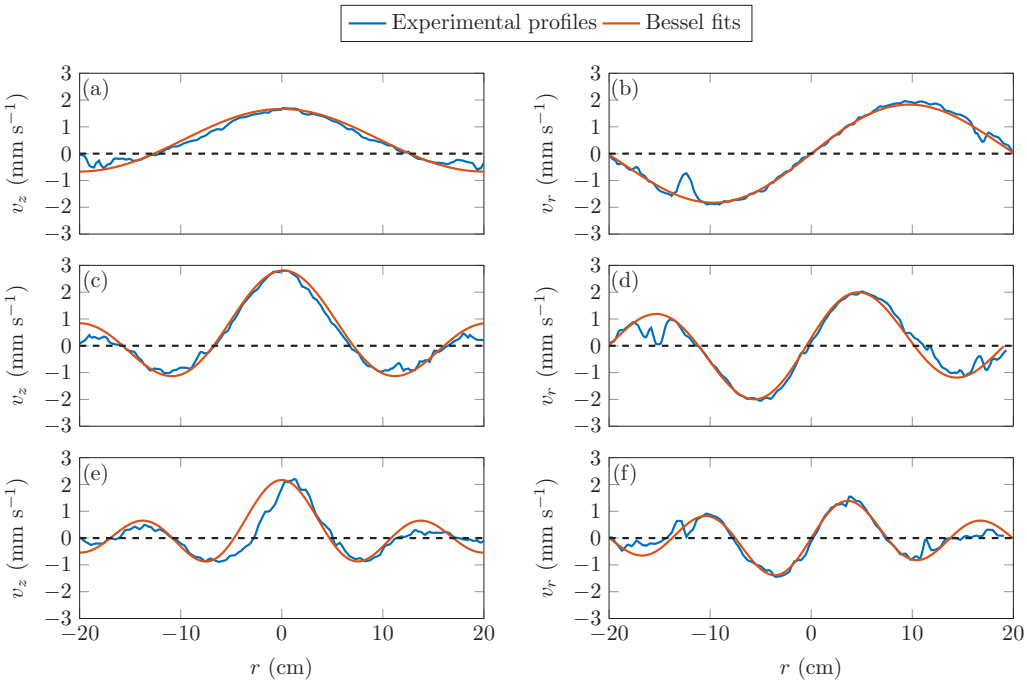

FIG. 5. From top to bottom: examples of experimental velocity profiles (left) v_z and (right) v_r for mode 1, mode 2, and mode 3, taken at a given time and altitude, fitted by appropriate Bessel functions: $J_0(lr)$ for v_z and $J_1(lr)$ for v_r, with $l = 19\,\mathrm{m}^{-1}$, $l = 35\,\mathrm{m}^{-1}$, and $l = 51\,\mathrm{m}^{-1}$ respectively.

The procedure to determine the wave amplitude was the following. In a first step, experimental amplitudes at a given time t_m were determined by fitting a Bessel function to the instantaneous horizontal profile at a given depth z_m of the vertical velocity, as illustrated in Fig. 5. The depth z_m chosen for this profile was selected to be 15 cm below the generator, as the wave field was properly developed at this depth. Since the stratification, the forcing frequency, and the radial wavelength are imposed, the only free parameter for the fit is the amplitude of the Bessel function. Note that we used the vertical component of the velocity field for this fitting, since it has larger amplitudes than the radial velocity profile (which is characterized by a node at $r = 0$) and so was more amenable to fitting.

Measurements were repeated for all images over a time interval $t_m \in [t_i; t_f]$, with t_i being the time when the wave is expected to first cross the horizontal cross section at $z = z_m$. The time t_f is the time when the reflected wave is predicted to reach $z = z_m$ after returning from the bottom of the tank, resulting in a disturbance of the wave field. Both t_i and t_f were estimated using the group velocity of the wave field established in Eq. (14). This series of measurements provided a time series of local wave amplitudes at $z = z_m$. An example of such a time series is shown in Fig. 6. One would expect this time signal to be sinusoidal. As can be seen in this example, the growth of the wave amplitude due to the presence of other frequencies associated with the ramping up of the wave generator can be observed for the first few periods, and the decay after t_f is due to the interfering waves returning out of phase. This illustrates the difficulty of wave amplitude measurement in a finite-size tank.

In a second step, in order to best estimate the wave amplitude of the steady state before the reflected wave returned (there is some uncertainty on the exact return time), we computed the RMS value of the time signal over three time-windows of one period length close to t_f half-covering each other, the middle one being just before theoretically seeing the reflected wave, the previous time-window covering the first half of this one, and the following time-window covering the second half of it (these measurement windows are illustrated by three rectangles in Fig. 6). The experimental

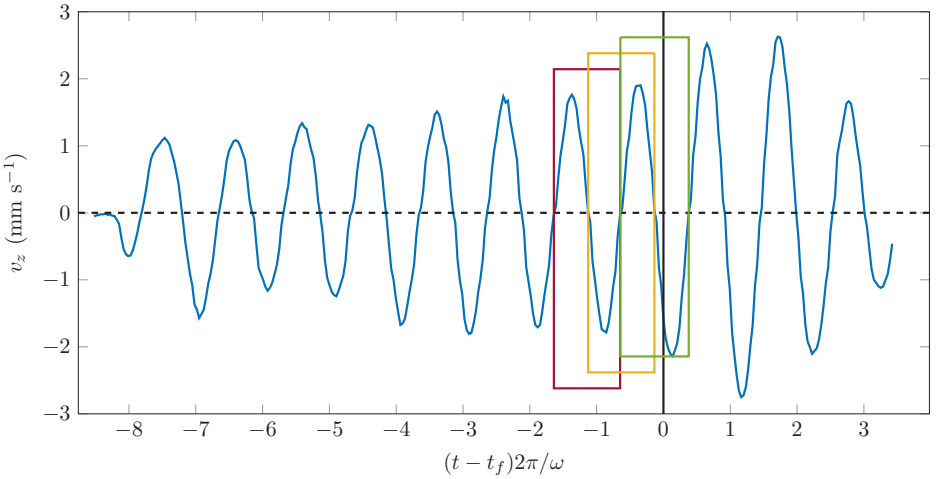

FIG. 6. Example of time series of fitted instantaneous Bessel function amplitudes of the vertical velocity, measured at $z = z_m = -15$ cm for a mode 1 wave. After identifying t_f (solid vertical line), three time-windows half-covering each other (rectangles) are used to extract the global wave amplitude *via* RMS estimates.

global amplitude was determined as the mean value of the three RMS values obtained (multiplied by $\sqrt{2}$), and the standard deviation of these three measurements gives an estimate of the associated error. We checked that the method was sound by repeating some test measurements for other horizontal planes and obtaining consistent results.

The results of our efficiency experiments are presented in Fig. 7 for two different generator amplitudes. We plot the velocity amplitude normalised by the generator velocity amplitude $a\omega$. From Eq. (37), without dissipation effects, one expects this ratio to be 1 (straight line in Fig. 7). This proves correct in the high-frequency range ($0.5 < \omega/N < 0.9$), except close to the buoyancy frequency as discussed further. The decrease at low frequency can be interpreted by viscous effects. Indeed, when one includes viscous dissipation in the theoretical development, the expression of the

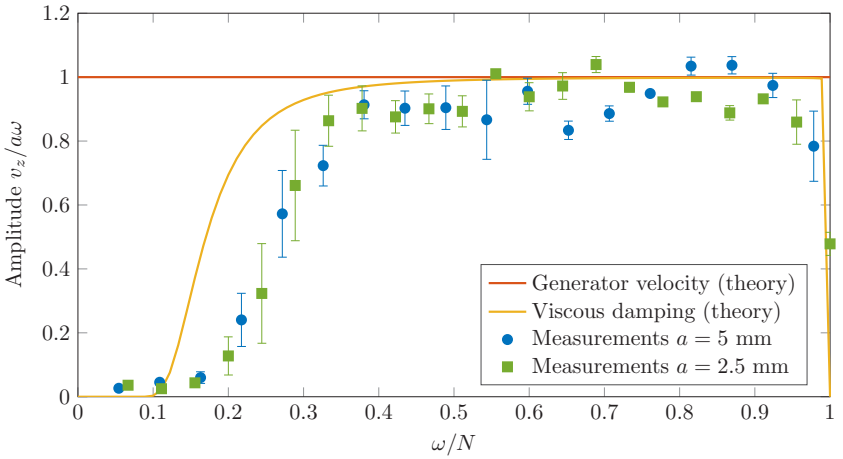

FIG. 7. Generator efficiency measured at $z = -15$ cm, for two experiments with $a = 5$ mm and $a = 2.5$ mm. Results are compared to the theoretical predictions in the inviscid case and in the weakly viscous case (viscous damping curve, computed for $N = 0.9$ rad s^{-1}).

stream function is given by Eq. (21). The curve corresponding to the vertical velocity extracted from this equation [at a depth of -15 cm since Eq. (21) depends on z] is plotted in Fig. 7, showing a similar behavior as the experimental data points for the two forcing amplitudes $a = 2.5$ mm and $a = 5$ mm. The difference in amplitude may be ascribed to boundary layer effects. Based on the approach of Beckebanze *et al.* [38], an order of magnitude calculation of the damping on the boundaries gives an estimate comparable to the dissipation in the bulk. At very low frequencies (below $\omega/N = 0.05$), the amplitude is so low that measurements become impossible. Finally, for $\omega/N = 0.9$ to 1, we notice a decrease in amplitude that is expected, as shown by the theoretical curve, since the waves are evanescent for $\omega/N > 1$. However, this decrease comes sooner than expected.

To conclude, the generator efficiency was investigated and shows a similar behavior as the theoretical prediction in all frequency ranges, providing one takes viscous effects into account. In addition, we identify a range of frequencies, from $\omega/N = 0.5$ to $\omega/N = 0.9$, where there is a very good agreement with the nonviscous theory, making this range suitable for axisymmetric modes experiment and for resonant enhancement.

C. Resonance

Having established the response of the stratification to the wave generator forcing, we then conducted experiments to detect resonance for a mode 1 excitation, due to the multiple reflections of the wave field at the top and bottom boundaries of the tank. These experiments consisted of measuring the amplitude of the wave by looking for the maximum value of vertical velocity in z and t at $r = 0$ [since $J_0(r = 0)$ is maximal and equal to 1]. The time window for these measurements was chosen to ensure the establishment of the steady state resonant wave field. In order to allow a minimum of about 10 back and forth crossings, we chose this time window to be from 280 s after starting the forcing, based on the minimum value of the group velocity of the waves, to 300 s, the end of the experiment duration.

Our experimental results are presented in Fig. 8, showing the measured velocity amplitude, normalized by the generator velocity amplitude $a\omega$. We performed two sets of experiments: one with $a = 2.5$ mm and $N \simeq 0.90\,\mathrm{rad\,s^{-1}}$ (blue circles) and another one with $a = 5$ mm and $N \simeq 0.88\,\mathrm{rad\,s^{-1}}$ (red squares). The first set of experiments was mainly aimed at identifying the resonant peaks; the second set was more evenly spread over all frequencies (100 values of ω/N from 0.625 to 1 at a regular interval). In the latter case, however, because of the larger generator amplitude, all experiments where the frequency was too close to the resonance led to strong nonlinear effects, making the measurement of an amplitude impossible. For this reason, the corresponding data points are not shown. The theoretical curve for the maximal amplitude of vertical velocity normalized by the generator, computed from Eq. (31), is also plotted in Fig. 8 as a solid line.

With the generator configured at low forcing amplitude ($a = 2.5$ mm), the peaks corresponding to the first resonant frequencies were observed as predicted by the theory (see Table I). The measured resonance peaks are not exactly centered on the predicted resonant frequencies, but this is not inconsistent with the characteristic 4% error on N. We see that in the vicinity of resonant frequencies the wave field reaches twice the amplitude of the generator, and even more for the highest frequencies. For nonresonant frequencies, however, the wave interaction is destructive, and the measured amplitude is half the amplitude of the generator.

In the vicinity of a resonant excitation frequency, we observed that the wave field amplitude kept strengthening until it triggered substantial nonlinear effects. To illustrate this, Fig. 9 presents the temporal evolution of a horizontal profile of the vertical velocity component for $\omega/N = 0.73$ [Fig. 9(a), nonresonant] and $\omega/N = 0.77$ [Fig. 9(b), resonant]. In the nonresonant case, each velocity profile has the shape of a Bessel profile, which is conserved during the whole experiment. No nonlinear deformation of the wave field can be observed. The beating behavior (i.e., low-frequency fading amplitude) is a transient state due to the fact that the reflected wave fields are not perfectly in phase, due to the nonresonance condition. In the resonant case, such oscillations do not exist as all reflections are in phase and interfere constructively. These reflections, however, lead to

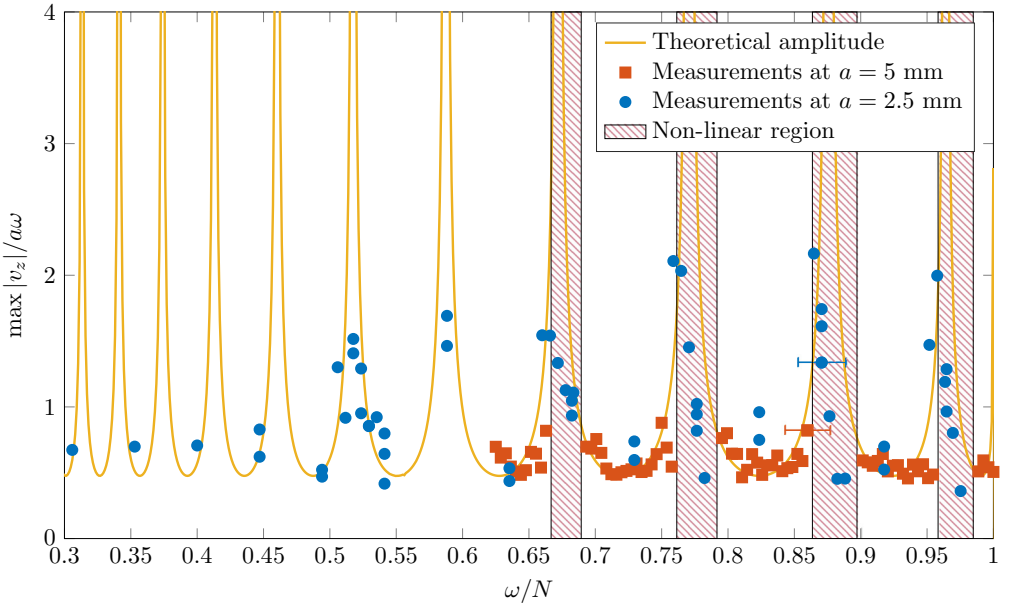

FIG. 8. Amplitude measurements of the vertical velocity in the resonant cavity normalized by the generator velocity amplitude. Yellow line: theoretical amplitude for an infinite sum of waves as a function of the frequency ω/N. The dots are from three different sets of measurements run for different buoyancies or amplitudes. Red hatched regions show intervals of frequencies in which nonlinear effects are clearly seen in the experiment for $a = 5$ mm.

an increasing amplitude that quickly triggers nonlinear effects in which waves at other frequencies than ω are excited, after 80 s in the example in Fig. 9(b). The Bessel axisymmetric shape of the profile starts to disappear from the center of the tank due to emerging nonlinear features, as the amplitude is maximum at $r = 0$. The nonlinearities then propagate radially towards the boundaries

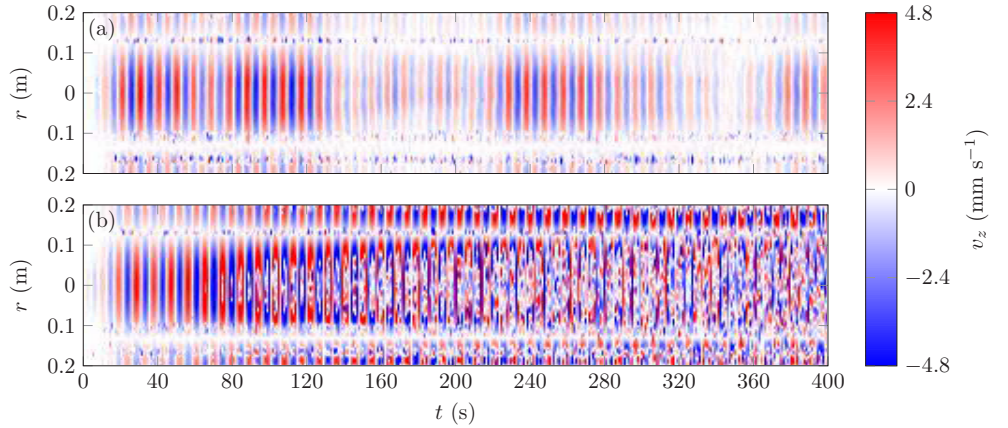

FIG. 9. Temporal evolution of a horizontal profile of vertical velocity located at the center of the tank, for (a) $\omega/N = 0.73$ (nonresonant case) and (b) $\omega/N = 0.77$ (resonant case). These profiles are measured at middepth in the tank for a mode 1 excitation, with $a = 5$ mm.

of the cylindrical tank, and the velocity field does not have a modal shape anymore [after 250 s in Fig. 9(b)].

By performing a similar analysis for all frequencies in the large-amplitude case ($a = 5$ mm), we identified four frequency ranges in which all experiments led to nonlinear effects. These ranges are marked with red hatched zones in Fig. 8. These intervals show a good agreement with the predicted resonance peaks (Table I) and with the increasing amplitude observed for the low-amplitude measurements ($a = 2.5$ mm).

V. CONCLUSIONS AND DISCUSSION

We have presented the results of a combined theoretical and experimental study of axisymmetric internal wave modes, in which we first developed the theoretical framework of radial standing waves propagating vertically in uniform stratifications, incorporating both radial and vertical confinement and accounting for the impact of weak viscous damping. Then we presented the results of a laboratory experimental study of axisymmetric internal wave mode generation. The effect of rotation was not explored in our experiments, but the governing equations predict qualitatively similar behavior as in the nonrotating case, the impact of rotation being foremost to influence the vertical wave number of the wave field for a given forcing frequency and buoyancy frequency [20,26]. The experimental wave fields were produced using a configuration of internal wave generator technology that has previously been primarily used to excite nominally planar wave fields; in our experiments the arrangement directly excited the Bessel functions that are the natural basis of cylindrical modes.

For the basic structure of the wave fields, there was very good qualitative and quantitative agreement between experiments and theory. Modes 1 through 3 were excited, leading to vertical and radial velocity profiles consistent with associated Bessel function forcing, and confirming the expected dispersion relation. As an additional component of these studies, we determined the efficiency of modal excitation by carefully studying the fluid system response to the generator forcing, fitting the PIV data to Bessel functions. A range of frequencies, from $\omega/N = 0.5$ to 0.9, was identified as being particularly suitable for studying axisymmetric modes as in this frequency range the wave field is attenuated very little and has an almost full response to the forcing amplitude of the generator.

Having established the ability to excite vertical modes, the role of vertical confinement was then investigated. Such confinement has the potential to generate a resonance effect when reflected modes constructively interfere with each other. The resonance conditions for our system were determined, and a series of experiments with different forcing amplitudes were performed. The experimental results on the wave field amplification aligned well with resonance predictions that incorporates weakly viscous correction for the wave field. Further refinement to account for the enhanced attenuation by boundary layers effects or the effects of near-surface and near-bottom homogeneous fluid layers due to the filling process or diffusion could account for the minor discrepancies observed. Within the bounds of resonant peaks, the wave field was seen to amplify sufficiently to trigger nonlinear effects that then eroded the linear wave field structure outwards from the centerline of the experimental domain, ultimately leading to a fully nonlinear wave field throughout the experimental domain.

While there have been a number of nominally two-dimensional experimental studies comparing plane wave or mode behavior with theoretical models, considering both their spatiotemporal form and transition to nonlinear phenomena, there have been few such studies for axisymmetric geometries, and most of them have been limited to the wave field excited by a vertically oscillating sphere. Axisymmetric wave fields are arguably more relevant as fundamental configurations for studying scenarios such as the excitation of atmospheric internal wave fields by storm cells [28] and the excitation of near-inertial wave fields in the ocean by surface storms [39]. This kind of laboratory experiments may also help to shed light on the resonance of seiches in appropriately shaped water basins, lakes, and estuaries [40,41]. The experimental apparatus and consequent studies presented

here demonstrate an ability to excite axisymmetric wave fields and pure radial modes, opening the path to investigation of linear (e.g., internal wave transmission) and nonlinear (e.g., TRI) internal wave phenomena in axisymmetric geometries. For example, inertial wave breaking and rotating turbulence, which was studied by Duran-Matute *et al.* [24] using an oscillating torus, could be further investigated using our configuration with any desired combination of Bessel modes.

ACKNOWLEDGMENTS

This work has been partially supported by the ANR through Grant No. ANR-17-CE30-0003 (DisET) and by ONR Physical Oceanography Grant No. N000141612450. S.B. thanks Labex iMust for supporting his research.

[1] H. Görtler, Über eine Schwingungserscheinung in Flüssigkeiten mit stabiler Dichteschichtung, Z. Angew. Math. Mech. **23**, 65 (1943).
[2] D. E. Mowbray and B. S. H. Rarity, A theoretical and experimental investigation of the phase configuration of internal waves of small amplitude in a density stratified liquid, J. Fluid Mech. **28**, 1 (1967).
[3] B. R. Sutherland, S. B. Dalziel, G. O. Hughes, and P. F. Linden, Visualization and measurement of internal waves by "synthetic schlieren." Part 1. Vertically oscillating cylinder, J. Fluid Mech. **390**, 93 (1999).
[4] D. A. Aguilar and B. R. Sutherland, Internal wave generation from rough topography, Phys. Fluids **18**, 066603 (2006).
[5] P. Echeverri, M. R. Flynn, K. B. Winters, and T. Peacock, Low-mode internal tide generation by topography: An experimental and numerical investigation, J. Fluid Mech. **636**, 91 (2009).
[6] M. J. Lighthill, On waves generated in dispersive systems by traveling forcing effects, with applications to the dynamics of rotating fluids, J. Fluid Mech. **27**, 725 (1967).
[7] B. R. Sutherland, *Internal Gravity Waves* (Cambridge University Press, Cambridge, 2010).
[8] D. Cacchione and C. Wunsch, Experimental study of internal waves over a slope, J. Fluid Mech. **66**, 223 (1974).
[9] S. A. Thorpe, On standing internal gravity waves of finite amplitude, J. Fluid Mech. **32**, 489 (1968).
[10] S. A. Thorpe, On the shape of progressive internal waves, Philos. Trans. R. Soc. London A **263**, 563 (1968).
[11] L. Gostiaux, H. Didelle, S. Mercier, and T. Dauxois, A novel internal waves generator, Exp. Fluids **42**, 123 (2006).
[12] D. Benielli and J. Sommeria, Excitation and breaking of internal gravity waves by parametric instability, J. Fluid Mech. **374**, 117 (1998).
[13] M. J. Mercier, D. Martinand, M. Mathur, L. Gostiaux, T. Peacock, and T. Dauxois, New wave generation, J. Fluid Mech. **657**, 308 (2010).
[14] S. Joubaud, J. Munroe, P. Odier, and T. Dauxois, Experimental parametric subharmonic instability in stratified fluids, Phys. Fluids **24**, 041703 (2012).
[15] Y. Dossmann, F. Pollet, P. Odier, and T. Dauxois, Mixing and formation of layers by internal wave forcing, J. Geophys. Res.: Oceans **122**, 9906 (2017).
[16] E. V. Ermanyuk, J.-B. Flór, and B. Voisin, Spatial structure of first and higher harmonic internal waves from a horizontally oscillating sphere, J. Fluid Mech. **671**, 364 (2011).
[17] M. R. Flynn, K. Onu, and B. R. Sutherland, Internal wave excitation by a vertically oscillating sphere, J. Fluid Mech. **494**, 65 (2003).
[18] S. J. Ghaemsaidi and T. Peacock, 3D stereoscopic PIV visualization of the axisymmetric conical internal wave field generated by an oscillating sphere, Exp. Fluids **54**, 1454 (2013).
[19] D. E. Mowbray and B. S. H. Rarity, The internal wave pattern produced by a sphere moving vertically in a density stratified liquid, J. Fluid Mech. **30**, 489 (1967).

[20] T. Peacock and P. Weidman, The effect of rotation on conical wave beams in a stratified fluid, Exp. Fluids **39**, 32 (2005).
[21] T. N. Stevenson, Axisymmetric internal waves generated by a traveling oscillating body, J. Fluid Mech. **35**, 219 (1969).
[22] B. Voisin, Limit states of internal waves beams, J. Fluid Mech. **496**, 243 (2003).
[23] A. M. J. Davis and S. G. L. Smith, Tangential oscillations of a circular disk in a viscous stratified fluid, J. Fluid Mech. **656**, 342 (2010).
[24] M. Duran-Matute, J.-B. Flór, F. S. Godeberd, and C. Jause-Labert, Turbulence and columnar vortex formation through inertial-wave focusing, Phys. Rev. E **87**, 041001(R) (2013).
[25] E. V. Ermanyuk, N. D. Shmakova, and J.-B. Flór, Internal wave focusing by a horizontally oscillating torus, J. Fluid Mech. **813**, 695 (2017).
[26] P. Maurer, S. J. Ghaemsaidi, S. Joubaud, T. Peacock, and P. Odier, An axisymmetric inertia-gravity wave generator, Exp. Fluids **58**, 143 (2017).
[27] B. Voisin, E. V. Ermanyuk, and J.-B. Flór, Internal wave generation by oscillation of a sphere, with application to internal tides, J. Fluid Mech. **666**, 308 (2011).
[28] M. Alexander, J. Holton, and D. Durran, The gravity-wave response above deep convection in a squall line simulation, J. Atmos. Sci. **52**, 2212 (1995).
[29] M. H. Alford, Internal swell generation: The spatial distribution of energy flux from the wind to mixed layer near-inertial motions, J. Phys. Oceanogr. **31**, 2359 (2001).
[30] J. D. Jackson, *Classical Electrodynamics*, 3rd. ed. (John Wiley & Sons, New York, 1999).
[31] F. Melde, Ueber die Erregung stehender Wellen eines fadenförmigen Körpers, Ann. Phys. **185**, 193 (1860).
[32] J. M. H. Fortuin, Theory and application of two supplementary methods of constructing density gradient columns, J. Polym. Sci. **44**, 505 (1960).
[33] G. Oster and M. Yamamoto, Density gradient techniques, Chem. Rev. **63**, 257 (1963).
[34] A. Fincham and G. Delerce, Advanced optimization of correlation imaging velocimetry algorithms, Exp. Fluids **29**, S013 (2000).
[35] M. Mathur and T. Peacock, Internal Wave Interferometry, Phys. Rev. Lett. **104**, 118501 (2010).
[36] P. Maurer, Approche expérimentale de la dynamique non-linéaire d'ondes internes en rotation, Ph.D. thesis, Université de Lyon, 2017.
[37] R. Supekar and T. Peacock, Interference and transmission of spatiotemporally locally forced internal waves in non-uniform stratifications, J. Fluid Mech. (to be published).
[38] F. Beckebanze, C. Brouzet, I. N. Sibgatullin, and L. R. M. Maas, Damping of quasi-two-dimensional internal wave attractors by rigid-wall friction, J. Fluid Mech. **841**, 614 (2018).
[39] M. H. Alford, Redistribution of energy available for ocean mixing by long-range propagation of internal waves, Nature (London) **423**, 159 (2003).
[40] M. I. Castillo, O. Pizarro, N. Ramírez, and M. Cáceres, Seiche excitation in a highly stratified fjord of southern Chile: The Reloncaví fjord, Ocean Sci. **13**, 145 (2017).
[41] S. Groeskamp, J. J. Nauw, and L. R. M. Maas, Observations of estuarine circulation and solitary internal waves in a highly energetic tidal channel, Ocean Dyn. **61**, 1767 (2011).